Structures of purine nucleosidase from *Trypanosoma brucei* bound to isozyme-specific trypanocidals and a novel metalorganic inhibitor

Francesca Giannese,[a] Maya Berg,[b] Pieter Van der Veken,[b] Valeria Castagna,[a] Paola Tornaghi,[a] Koen Augustyns[b] and Massimo Degano[a]*

[a]Biocrystallography Unit, Department of Immunology, Transplantation and Infectious Diseases, Scientific Institute San Raffaele, via Olgettina 58, 20132 Milano, Italy, and [b]Laboratory of Medicinal Chemistry, University of Antwerp, Universiteitsplein 1, 2610 Antwerp, Belgium

Correspondence e-mail: degano.massimo@hsr.it

Sleeping sickness is a deadly disease that primarily affects sub-Saharan Africa and is caused by protozoan parasites of the *Trypanosoma* genus. Trypanosomes are purine auxotrophs and their uptake pathway has long been appreciated as an attractive target for drug design. Recently, one tight-binding competitive inhibitor of the trypanosomal purine-specific nucleoside hydrolase (IAGNH) showed remarkable trypanocidal activity in a murine model of infection. Here, the enzymatic characterization of *T. brucei brucei* IAGNH is presented, together with its high-resolution structures in the unliganded form and in complexes with different inhibitors, including the trypanocidal compound UAMC-00363. A description of the crucial contacts that account for the high-affinity inhibition of IAGNH by iminoribitol-based compounds is provided and the molecular mechanism underlying the conformational change necessary for enzymatic catalysis is identified. It is demonstrated for the first time that metalorganic complexes can compete for binding at the active site of nucleoside hydrolase enzymes, mimicking the positively charged transition state of the enzymatic reaction. Moreover, we show that divalent metal ions can act as noncompetitive IAGNH inhibitors, stabilizing a nonproductive conformation of the catalytic loop. These results open a path for rational improvement of the potency and the selectivity of existing compounds and suggest new scaffolds that may be used as blueprints for the design of novel antitrypanosomal compounds.

1. Introduction

Sleeping sickness is a parasitic disease caused by protozoa of the species *Trypanosoma brucei*. This pathology is endemic in sub-Saharan Africa, where its incidence is second only to HIV/AIDS, with frequent outbreaks in Central Africa; an estimated 0.5 million individuals are infected and more than 70 000 new cases are reported per year (World Health Organization, 2006). The disease is fatal if not treated, as parasites initially multiply in the blood and lymph and ultimately invade the central nervous system (John & Petri, 2006). Successful clearance of the infection crucially depends on an early diagnosis and treatment with a limited set of trypanocidals (for instance, pentamidine and suramin). Indeed, only a few compounds (such as eflornithine and melarsoprol) are endowed with significant antitrypanosomal activity and can cross the blood–brain barrier. The latter drug often displays severe side effects on the host owing to a strong systemic toxicity that results in death in up to 10% of treated cases (World Health Organization, 1998). Moreover, cases of drug resistance of trypanosomes have been reported in several studies (Brun *et al.*, 2011; Legros *et al.*, 1999). Hence, there is

a continuous and urgent need for new drugs against this neglected disease that are directed at new molecular targets and are endowed with higher efficacy and safety.

Nucleotide metabolism in trypanosomes has long drawn attention for the development of novel trypanocidal compounds (Barrett *et al.*, 1999; Berens *et al.*, 1981). Indeed, trypanosomes are purine-auxotrophic, lacking the enzymatic activities required for *de novo* synthesis, as appreciated from both biochemical (Hammond & Gutteridge, 1984) and genomic analyses (Berriman *et al.*, 2005). Thus, these parasites rely on an intricate and highly efficient uptake and recycling system for nitrogenous bases (Berg, Van der Veken *et al.*, 2010; James & Born, 1980). In trypanosomes, extracellular nucleotidases act in conjunction with nucleoside transporters to import the neutral ribosides into the cell (de Koning *et al.*, 2005). Cellular nucleosides can then either follow a direct phosphorylation to the mononucleotide (Ogbunude *et al.*, 1985) or undergo N-glycosidic bond cleavage to release the nitrogenous base (Hammond & Gutteridge, 1984). In the latter case, the free base can be incorporated into mononucleotides *via* a phosphoribosyl transferase-catalyzed reaction. Phosphorylation is mediated by high-affinity nucleoside kinases, epitomized by the adenosine kinase enzyme (AK; Vodnala *et al.*, 2008). AK inhibitors have been shown to have trypanocidal activity and are thus of potential interest for drug design (Kuettel *et al.*, 2009, 2011). However, the AK enzyme is

also present in humans and shares high structural similarity with the trypanosomal counterpart. Thus, the possibility of cross-reactivity, and thereby low selectivity, poses challenging issues for the development of AK inhibitors as effective trypanocidal compounds.

In trypanosomes, more than 75% of the exogenously provided nucleosides undergo N-glycosidic bond cleavage (Estupiñán & Schramm, 1994; Ogbunude *et al.*, 1985). This reaction is catalyzed exclusively by nucleoside hydrolases (NHs), a class of enzymes that are widespread in all kingdoms of life but are notably absent in mammals (Giabbai & Degano, 2004; Gopaul *et al.*, 1996). Humans instead employ the structurally and functionally distinct nucleoside phosphorylases in nitrogenous base catabolism (Tsuboi & Hudson, 1957). Hence, NHs have long been appreciated as potential attractive targets for antitrypanosomal drug design, being unique to the parasite and distinct from host enzymes. NHs are Ca^{2+}-dependent glycosyl hydrolases that are strictly specific for ribonucleoside substrates. The specificity towards nitrogenous bases varies among different NH isozymes and is determined by the architecture of the active site, which is optimized for the binding of substrate and the stabilization of the transition state (Degano *et al.*, 1998; Iovane *et al.*, 2008; Versées *et al.*, 2001, 2004; Versées & Steyaert, 2003). Two NH enzymes specific for purine nucleosides have been identified in *T. brucei brucei*, which is a close model of the human pathogens *T. brucei rhodesiense* and *T. brucei gambiense*: an inosine–guanosine-preferring enzyme (IGNH; Parkin, 1996; Vandemeulebroucke *et al.*, 2010) and a purine-specific nucleosidase (inosine–adenosine–guanosine-preferring; IAGNH; Parkin, 1996).

Owing to the great interest in trypanosomal NH inhibition for the development of lead compounds, several tight-binding inhibitors have been engineered and synthesized. The C1′-substituted iminoribitols (immucillins; Fig. 1) were based on the characteristics of the transition state of the enzymatic reaction (Horenstein & Schramm, 1993; Miles *et al.*, 1999; Parkin *et al.*, 1997) and display subnanomolar inhibition constants (K_i) towards IAGNH (Parkin, 1996). These molecules are cross-reactive with human purine nucleoside phosphorylase (Schramm, 2002), an enzyme whose genetic absence leads to severe combined immunodeficiency (Giblett *et al.*, 1975). A clinical study reported an immucillin-induced neutropaenia (Gandhi *et al.*, 2005) that may enhance the risk of life-threatening bacterial infections. On the other hand, a more recent analysis showed that these compounds are effective in eradicating a primate model of *Plasmodium falciparum* infection without noticeable side effects (Cassera *et al.*, 2011). Since higher doses of the immucillins may be required to kill the trypanosomes, which have a distinct life cycle compared with the malaria-causing *Plasmodium*, compounds with higher selectivity have been devised in order to avoid detrimental effects on the host upon treatment. A family of N4′-linked arylmethyl iminoribitols that were designed based on the structure of the purine-specific NH from the cattle pathogen *T. vivax* (TvIAGNH) are tight-binding inhibitors and are highly selective for the trypanosomal hydrolases (Goeminne *et al.*, 2008). The latter molecules
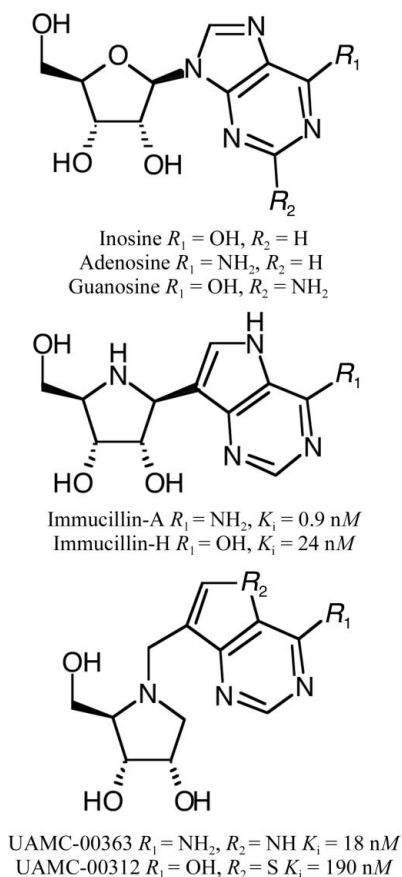

Inosine R_1 = OH, R_2 = H
Adenosine R_1 = NH$_2$, R_2 = H
Guanosine R_1 = OH, R_2 = NH$_2$

Immucillin-A R_1 = NH$_2$, K_i = 0.9 nM
Immucillin-H R_1 = OH, K_i = 24 nM

UAMC-00363 R_1 = NH$_2$, R_2 = NH K_i = 18 nM
UAMC-00312 R_1 = OH, R_2 = S K_i = 190 nM

Figure 1
Chemical structures of the C1′-substituted iminoribitols (immucillins).

also bind to both IGNH and IAGNH from *T. brucei brucei*, and compound UAMC-00363 shows a trypanocidal activity comparable to that of pentamidine or suramin both *in vitro* and in *in vivo* models of infection. This effect is mediated by both inhibition of the purine-specific NH enzymes and the interaction with an as yet unidentified target (Berg, Kohl *et al.*, 2010). Notably, the arylmethyl iminoribitols display lower affinity for *T. brucei brucei* IGNH and IAGNH compared with TvIAGNH, underscoring the need for detailed knowledge of the three-dimensional structure of the target enzyme from the human pathogen for the optimal design of specific inhibitors.

Here, we report a functional and structural study of IAGNH from *T. brucei brucei*. The high-resolution structural characterization of the protein both in the unliganded form and in complexes with three iminoribitol-based competitive inhibitors (UAMC-00363, immucillin-A and UAMC-00312) reveals crucial contacts that can be exploited for the design of high-affinity inhibitors. We demonstrate for the first time that NH enzymes can be inhibited by transition metals and metal-organic compounds through both competitive and noncompetitive mechanisms and provide a structural basis for this novel finding. The distinct conformations of the IAGNH protein induced by different ligands shed light on the mechanism that leads to attainment of the catalytic conformation. Our results widen the horizon of structural targets to be exploited for the synthesis of efficient antitrypanosomal compounds.

2. Methods

2.1. Cloning, expression and purification

The 1097 bp IAGNH-encoding gene (Gene ID 3656230) from the *T. brucei brucei* (TREU927) genome was identified through homology searches using the *T. vivax* IAGNH sequence as a template. The IAGNH gene was cloned using standard PCR methodology with genomic DNA as template and gene-specific primers including *Nde*I and *Xho*I recognition sequences at the extremities. The purified PCR product was cloned between the *Nde*I and *Xho*I restriction sites of the pET28b vector (Novagen) and transformed into *Escherichia coli* BL21(DE3) cells for protein expression. Cells were grown at 310 K in Luria–Bertani medium supplemented with 50 µg ml^{-1} kanamycin with shaking at 210 rev min^{-1}. Protein expression was induced by the addition of 0.5 m*M* isopropyl β-D-1-thiogalactopyranoside (IPTG) when the optical density of the culture at 600 nm reached 0.7, followed by 16 h incubation at room temperature. Cells were harvested by centrifugation and the pellet was resuspended in a 1/10 volume of 20 m*M* Tris pH 8.0, 50 m*M* NaCl supplemented with 1 mg ml^{-1} lysozyme, 20 µg ml^{-1} RNAse A and 2 µg ml^{-1} DNAse I. Cells were disrupted by sonication and the soluble fraction was recovered after centrifugation. The clarified soluble extract was incubated with Ni–NTA resin (Qiagen) and the bound proteins were eluted with a buffer consisting of 20 m*M* Tris pH 8, 0.5 *M* NaCl, 0.5 *M* imidazole. The N-terminal hexahistidine tag was proteolytically removed by incubating the protein with

thrombin (Sigma) at a 1:500(*w:w*) ratio for 9 h at room temperature. The reaction mixture was applied onto a Superdex 200 10/30 size-exclusion chromatography column coupled to an ÄKTApurifier 10 (GE Healthcare) and isocratically eluted using 20 m*M* HEPES pH 7.4, 150 m*M* NaCl. Molecular weights were estimated from the elution volumes using a calibration curve derived from known standards. Dynamic light-scattering measurements were performed with a DynaPro MS-X instrument, optimizing the laser intensity, time and number of measurements in order to avoid detector saturation. The protein was concentrated using ultrafiltration devices. Protein concentration was determined spectrophotometrically using a calculated molar absorption coefficient of 48 190 *M*$^{-1}$ cm^{-1} at 280 nm (Pace *et al.*, 1995).

2.2. Kinetic characterization and inhibition

Steady-state kinetic parameters were determined using a spectrophotometric assay, taking advantage of the difference in absorbance between the nucleoside and the corresponding base at a specific wavelength. The $\Delta\varepsilon$ coefficients used are reported in Supplementary Table S1[1]. For the substrate uridine, the NH colorimetric assay based on reducing sugar was employed (Parkin *et al.*, 1991). Reactions were started by the addition of the substrate at the desired concentration to a buffer consisting of 50 m*M* HEPES pH 7.3 and the enzyme and were monitored using an UltroSpec2100 spectrophotometer (GE Healthcare) at the appropriate wavelength at a temperature of 310 K. Initial rates were derived from the progress curves with less than 10% conversion of substrate. Initial velocities were fitted to the Michaelis–Menten equation using *GraphPad Prism* 5 (GraphPad Software Inc.). Inhibition constants for metalorganic compounds and transition-metal ions were determined by full kinetic analysis using inosine as a substrate and three different inhibitor concentrations at the required pH. For competitive inhibition, data were fitted to the equation

$$K_{\mathrm{m}}^{*} = K_{\mathrm{m}}\left(1 + \frac{[\mathrm{I}]}{K_{\mathrm{i}}}\right). \quad (1)$$

In the case of noncompetitive and mixed-type inhibition, the apparent maximal velocity (V_{max}^{*}) and Michaelis constant (K_{m}^{*}) were fitted to the equations

$$V_{\mathrm{max}}^{*} = \frac{V_{\mathrm{max}}}{1 + \dfrac{[\mathrm{I}]}{K_{\mathrm{ii}}}}, \quad (2)$$

$$K_{\mathrm{m}}^{*} = K_{\mathrm{m}}\left(1 + \frac{[\mathrm{I}]}{K_{\mathrm{i}}}\middle/ 1 + \frac{[\mathrm{I}]}{K_{\mathrm{ii}}}\right), \quad (3)$$

where K_{m} and V_{max} are the Michaelis constant and the maximal velocity for inosine in the absence of inhibitor, respectively, [I] is the inhibitor concentration and K_{i} and K_{ii}

---

[1] Supplementary material has been deposited in the IUCr electronic archive (Reference: MH5087). Services for accessing this material are described at the back of the journal.

Table 1
Crystallographic data-collection and refinement statistics.

	IAGNH	IAGNH-363	IAGNH-ImmA	IAGNH-312	IAGNH-312-M	IAGNH-NiTris
PDB code	4i70	4i71	4i72	4i73	4i74	4i75
Data collection						
Unit-cell parameters (Å, °)	$a = b = 48.04$, $c = 216.11$	$a = 66.36$, $b = 72.35$, $c = 133.28$	$a = 72.75$, $b = 130.98$, $c = 63.69$	$a = 63.17$, $b = 131.67$, $c = 71.85$, $\beta = 91.33$	$a = 60.12$, $b = 69.42$, $c = 130.23$	$a = 70.74$, $b = 134.96$, $c = 61.03$
Space group	$P3_212$	$C222_1$	$P2_12_12$	$P2_1$	$C222_1$	$P2_12_12$
Wavelength (Å)	0.976	0.976	0.933	0.933	0.933	0.870
Resolution range (Å)	72–1.60 (1.70–1.60)	133.3–1.28 (1.32–1.28)	50–1.99 (2.10–2.05)	50–2.18 (2.24–2.18)	45.45–1.68 (1.72–1.68)	49–1.80 (1.85–1.80)
Measured reflections	373641 (46780)	267904 (5578)	284249 (20887)	230362 (16007)	220843 (14873)	200743 (13424)
Unique reflections	38235 (6215)	78467 (3472)	38963 (2831)	61007 (4374)	31441 (2283)	54442 (3780)
Multiplicity	9.8 (7.5)	3.4 (1.6)	7.3 (7.4)	3.8 (3.7)	7.0 (6.5)	3.7 (3.5)
Completeness (%)	99.7 (99.3)	95.8 (57.8)	100 (100)	99.7 (97.5)	99.9 (99.2)	99.4 (95.5)
R_{merge}†	0.099 (0.389)	0.048 (0.264)	0.098 (0.690)	0.138 (0.671)	0.083 (0.657)	0.068 (0.561)
R_{meas}‡	0.104 (0.418)	0.054 (0.353)	0.105 (0.743)	0.161 (0.786)	0.089 (0.711)	0.080 (0.660)
$\langle I/\sigma(I)\rangle$	22.50 (5.94)	16.64 (2.84)	18.39 (3.03)	9.06 (1.96)	18.94 (2.94)	14.29 (2.60)
Wilson B factor (Å^2)	18.4	11.9	24.2	23.7	15.0	26.3
Refinement statistics						
Resolution range (Å)	72.0–1.60	133.3–1.28	47.9–2.00	71.8–2.18	42.9–1.68	49.0–1.80
No. of reflections, $F > 0$	38232	78467	38960	61007	31439	54442
No. used for R_{free}	1916	3944	1590	3089	1590	2761
R_{cryst}§	0.142	0.126	0.177	0.200	0.150	0.180
R_{free}¶	0.182	0.147	0.234	0.248	0.188	0.223
R.m.s.d. bonds (Å)	0.016	0.019	0.016	0.017	0.015	0.015
R.m.s.d. angles (°)	1.536	1.748	1.558	1.601	1.579	1.422
Ramachandran plot, residues in (%)						
Core regions	91.3	90.9	89.8	90.6	91.3	92.4
Allowed regions	8.4	8.7	9.9	9.3	8.3	7.2
Generously allowed regions	0.4	0.3	0.3	0.1	0.3	0.2
Disallowed regions	0.0	0.0	0.0	0.0	0.0	0.2
Average B factors (Å^2)						
Protein	18.0	13.9	31.3/31.6	23.3/23.2/23.3/23.3	19.8	19.9/20.7
Ligand	—	8.6	25.6/32.6	19.0/18.8/18.9/19	16.6	14.0/15.7
Solvent	27.9	22.5	37.8	24.9	29.2	18.7

† $R_{merge} = \sum_{hkl}\sum_i |I_i(hkl) - \langle I(hkl)\rangle|/\sum_{hkl}\sum_i I_i(hkl)$, where $I_i(hkl)$ and $\langle I(hkl)\rangle$ are the intensities of the ith measurement and the average value for reflection hkl, respectively. ‡ R_{meas} is the multiplicity-weighted R_{merge}. § $R_{cryst} = \sum_{hkl} ||F_{obs}| - |F_{calc}||/\sum_{hkl} |F_{obs}|$, where F_{obs} and F_{calc} are the observed and calculated structure factors for reflection hkl, respectively. ¶ R_{free} is calculated as R_{cryst} but using a subset of reflections that were randomly selected after data reduction and excluded from all stages of refinement.

are the dissociation constants of the EI and ESI complexes, respectively.

2.3. Formation of metalorganic complexes

2-Amino-2-(hydroxymethyl)-1,3-propanediol (Tris), 4-(2-hydroxyethyl)piperazine-1-ethanesulfonic acid (HEPES), glycylglycine and transition-metal chloride salts (Mn^{2+}, Co^{2+}, Ni^{2+}, Cu^{2+} and Zn^{2+}) were purchased from Sigma. Iron was not included in the analysis owing to its poor solubility at basic pH. Salts were dissolved in distilled water and mixed with the appropriate ligand at the required molar ratio and pH. Absorption spectra in the UV–Vis region (200–900 nm) were recorded using an UltroSpec 2100 (GE Healthcare) with a 1 cm cuvette at room temperature.

2.4. Crystallization and data collection

The IAGNH protein was concentrated to 140 µM for crystallization experiments. The complexes with iminoribitol-based compounds were prepared by incubation of the protein with a threefold molar excess of ligand (calculated per protein active site). IAGNH was crystallized using the hanging-drop vapour-diffusion method by mixing equal volumes of protein and precipitant solution (Supplementary Table S2) at 289 K.

Diffraction data were collected on the beamlines of the European Synchrotron Radiation Facility, Grenoble, France at 100 K using a fixed wavelength and the oscillation method. Prior to collection, the crystals were transferred into a cryo-protecting solution corresponding to the mother liquor with the concentration of PEG or PEG MME increased to 34%, equilibrated for 10 min and rapidly dipped into liquid nitrogen. Data were indexed, integrated, scaled and reduced to unique reflections using *XDS* (Kabsch, 2010a). Structure factors were computed using *TRUNCATE* (French & Wilson, 1978). Space groups were assigned based on symmetries in the diffraction pattern and systematic absences (Kabsch, 2010b), and the choice between enantiomorphic space groups was based on the molecular-replacement results. A summary of crystal and data-collection parameters is presented in Table 1.

2.5. Structure solution and refinement

For the IAGNH-363 complex (see Supplementary Table S2 for nomenclature), the initial phases were obtained using the molecular-replacement method as implemented in *MOLREP* (Vagin & Teplyakov, 2010). The rotation and translation functions were calculated using data to 3.5 Å resolution and the unliganded IAGNH from *T. vivax* (PDB entry 1kic;

Table 2
Steady-state kinetic parameters for IAGNH from *T. brucei brucei* (Tbb) and a comparison with other purine-specific trypanosomal isozymes.

	TbbIAGNH			TbbIGNH†			TvIAGNH‡		
	k_{cat} (s^{-1})	K_m (μM)	k_{cat}/K_M (M^{-1} s^{-1})	k_{cat} (s^{-1})	K_m (μM)	k_{cat}/K_M (M^{-1} s^{-1})	k_{cat} (s^{-1})	K_m (μM)	k_{cat}/K_M (M^{-1} s^{-1})
Inosine	61 ± 1	51 ± 2	$(1.19 \pm 0.01) \times 10^6$	28	1.9	1.5×10^7	5.2	5.37	9.7×10^5
Adenosine	17.3 ± 0.4	16 ± 1	$(1.09 \pm 0.04) \times 10^6$	0.273	<1	$>2.4 \times 10^5$	1.5	8.54	1.7×10^5
Guanosine	37.3 ± 1.9	75 ± 12	$(4.99 \pm 0.07) \times 10^5$	37.6	4.5	8.3×10^6	1.9	3.82	4.8×10^5
Cytidine	0.27 ± 0.01	240 ± 28	$(1.12 \pm 0.01) \times 10^3$	0.52	271	1.9×10^3	0.338	925	3.7×10^2
Uridine	0.01 ± 0.001	254 ± 91	$(3.90 \pm 0.30) \times 10^1$	0.0038	1451	2.6	0.022	586	3.8×10^1
pNPR	0.048 ± 0.001	713 ± 62	$(6.73 \pm 0.03) \times 10^1$	0.030	1.1	2.7×10^4	0.206	257	8.0×10^2

† Vandemeulebroucke *et al.* (2010).   ‡ Versées *et al.* (2001).

Versées *et al.*, 2001) as a search model after removing all solvent molecules and ions and truncating all nonglycine residues to alanine to minimize model bias. The correct solutions were evident from the correlation coefficients and *R* factors and were confirmed by inspection of difference electron-density maps, which showed a positive peak at each active site corresponding to the trademark Ca^{2+} ion. The model was rebuilt using *ARP/wARP* (Cohen *et al.*, 2008; Perrakis *et al.*, 1997). Active-site ions and ligands were included as suggested from the initial electron-density maps. Refinement of the model proceeded by rounds of restrained maximum-likelihood minimization as implemented in *REFMAC*5 (Murshudov *et al.*, 2011) followed by manual adjustment in electron-density maps calculated with $2mF_o - DF_c$ and $mF_o - DF_c$ coefficients and model phases using the program *Coot* (Emsley & Cowtan, 2004; Emsley *et al.*, 2010). Alternative conformations of amino-acid side chains were modelled and solvent molecules were added to spherical peaks of $>3\sigma$ in the difference maps. Anisotropic temperature factors were refined in the later stages of refinement. Alternative conformations of amino-acid side chains were included when suggested by residual difference density and were confirmed after refinement. The final model contains residues 1–327 of IAGNH, excluding residues 298–302, which lacked corresponding electron density. The model also contains a Gly-Ser-His tripeptide at the N-terminus originating from the engineered thrombin-recognition site that had clear associated electron density, one Ca^{2+} ion at the active site, four Ni^{2+} ions and one Tris molecule from the crystallization buffer.

For apo IAGNH and the other complexes, the procedure was repeated independently but using the refined IAGNH-363 model to obtain initial phases with the molecular-replacement method. Anisotropic motion of the atoms was modelled for the unliganded IAGNH (Murshudov *et al.*, 1999), while an isotropic model was used for the other structures. The apo IAGNH model lacks the region spanning amino-acid residues 245–255, which was highly flexible and was not traceable in the electron-density maps. The structure of the 312-M complex showed residual density at the active site consistent with partial occupation by Ni–Tris, which was modelled by the addition of a metalorganic complex molecule with an occupancy of 0.20. In the 312-M structure the presence of the noncompetitive inhibitor Ni^{2+} was confirmed using an anomalous difference map calculated from the same data set with

the Bijvoet pairs unmerged and model phases. The ion is located close to the crystallographic twofold axis and its position is unstable during refinement, possibly owing to static disorder. Following the indications of the residual density map, we thus introduced two Ni^{2+} ions into the asymmetric unit with an occupancy of 0.25. For the structural analysis, we positioned an Ni^{2+} ion at the centroid of the four ions present in the model after applying crystallographic symmetry. The polypeptide chains used for the structural analysis presented here correspond to chain *A* in all of the deposited files, except for IAGNH-NiTris, where chain *B* was used. The quality of the models was continuously monitored using the *MolProbity* server (Chen *et al.*, 2010) and the geometrical analysis of the final models is reported in Table 1. Buried surface areas were calculated using *AREAIMOL* (Lee & Richards, 1971) and enzyme–ligand contacts and hydrogen bonds were determined using *CONTACT*, which are both part of the *CCP*4 suite (Winn *et al.*, 2011). The intensity distribution of the IAGNH-312 complex was suggestive of possible merohedral twinning using the $(-h, -k, l)$ operator and a twinning fraction of 0.11. However, inclusion of twin refinement with *REFMAC* did not improve the electron-density maps and resulted in only a minor decrease in the *R* factors. We therefore concluded that the intensity distributions were affected by the noncrystallographic symmetry axes parallel to the crystallographic axis. All refined models and structure factors have been deposited in the Protein Data Bank (PDB codes are given in Table 1).

3. Results

3.1. Characterization of IAGNH from *T. brucei brucei*

We identified two genes in the *T. brucei brucei* genome coding for proteins with NH-like properties: an inosine–adenosine–guanosine-specific enzyme (IAGNH) and a 6-oxo-purine-specific enzyme (IGNH) (Vandemeulebroucke *et al.*, 2010). The IAGNH gene is composed of a 984 bp open reading frame located on chromosome 3 (accession No. XM_838796) corresponding to a polypeptide of 327 amino acids. The deduced amino-acid sequence of the cloned IAGNH gene is identical to the corresponding protein from the human pathogen *T. brucei gambiense* (Jackson *et al.*, 2010). The IAGNH shares 68% identity with the TvIAGNH enzyme, but only shares 10% identity with the IGNH enzyme. In

Table 3
Inhibition of IAGNH by transition metals and metal–Tris coordination complexes.

Competitive (K_i) and noncompetitive (K_{ii}) inhibition constants of transition metals (values in parentheses were measured in the presence of Tris). The formation of the M^{2+}–Tris complex reduces the K_i owing to its higher affinity towards IAGNH, with the exception of Mn^{2+}. Addition of Tris instead increases the K_{ii} values owing to the reduction of free ions in solution. Precise values for K_{ii} in the presence of M^{2+}–Tris could only be accurately determined for Cu^{2+} owing to the high apparent K_m under the assay conditions. Mixed inhibition was nevertheless apparent from the analysis of double-reciprocal plots.

Ion	Inhibition type	K_i (µM)	K_{ii} (µM)
Mn^{2+}	Mixed	290 ± 57 ($>10^3$)	$>10^3$ ($>10^3$)
Co^{2+}	Mixed	160 ± 40 (11.2 ± 2.5)	$>10^3$ ($>10^3$)
Ni^{2+}	Mixed	28 ± 6 (3.4 ± 0.4)	390 ± 36 ($>10^3$)
Cu^{2+}	Noncompetitive	—	0.9 ± 0.1 (840 ± 60)
Zn^{2+}	Mixed	2.8 ± 0.5 (4.0 ± 0.5)	16.7 ± 0.7 ($>10^3$)

accordance with previous studies (Parkin, 1996), the protein displays an apparent homodimeric structure, as judged from its elution profiles in size-exclusion chromatography and dynamic light-scattering experiments (not shown).

3.2. Enzymatic activity of IAGNH

The IAGNH enzyme was assayed for nucleosidase activity on purine, pyrimidine and synthetic nucleosides (Table 2). The enzyme displays a strict specificity for purine nucleosides, with specificity constants (k_{cat}/K_m) ranging from 10^2-fold to 10^4-fold higher compared with pyrimidine ribosides. Indeed, the lower K_m values and higher turnover numbers (k_{cat}) for purine nucleosides reflect a highly optimized active site for both specific binding and catalysis. The synthetic compound para-nitrophenyl riboside (pNPR) is a poor substrate for IAGNH, with a high micromolar K_m and low turnover number, implying that IAGNH obtains its catalytic power primarily through leaving-group activation (Mazzella et al., 1996). The kinetic constants of the recombinant IAGNH are consistent with those reported previously for the purified enzyme (Parkin, 1996) and are similar to those of the homologous isozyme TvIAGNH, thus reflecting a conserved physiological function in these closely related parasites (Table 2).

3.3. Inhibition of IAGNH by divalent cations and coordination complexes

We characterized the effect of several divalent metal ions (Mn^{2+}, Co^{2+}, Ni^{2+}, Cu^{2+} and Zn^{2+}) on the activity of IAGNH (Table 3). All ions tested inhibit IAGNH through a mixed-type mechanism, with the exception of Cu^{2+}, which yielded exclusively noncompetitive inhibition with a submicromolar K_{ii} value. We then measured the K_{ii} of Cu^{2+} ions at different pH values, revealing that tight binding occurs at basic pH, which is apparently a consequence of the deprotonation of one or more amino-acid residues endowed with near-neutral pK_a. Since Tris buffer is capable of forming coordination complexes in solution with transition-metal ions (Allen et al., 1967; Hall et al., 1962; Fischer et al., 1979), we investigated

whether the observed inhibition of IAGNH could be modulated by this organic compound. Tris itself is a poor competitive inhibitor of IAGNH at neutral pH, with a K_i value of 41 mM; however, this decreases to 14.2 mM at pH 8.2 and to 1.2 mM at pH 8.5. We characterized the interaction between Ni^{2+} and Tris, confirming maximal complex formation at basic pH values, which is likely to be a consequence of the protonation state of the Tris molecule (Fig. 2). The formation of coordination complexes was quantitative with a tenfold molar excess of Tris at pH 8.5. The ability of the other transition-metal ions to form coordination complexes with Tris was similarly tested (data not shown). In the presence of Tris at pH 8.2, the inhibition of IAGNH by divalent cations changes
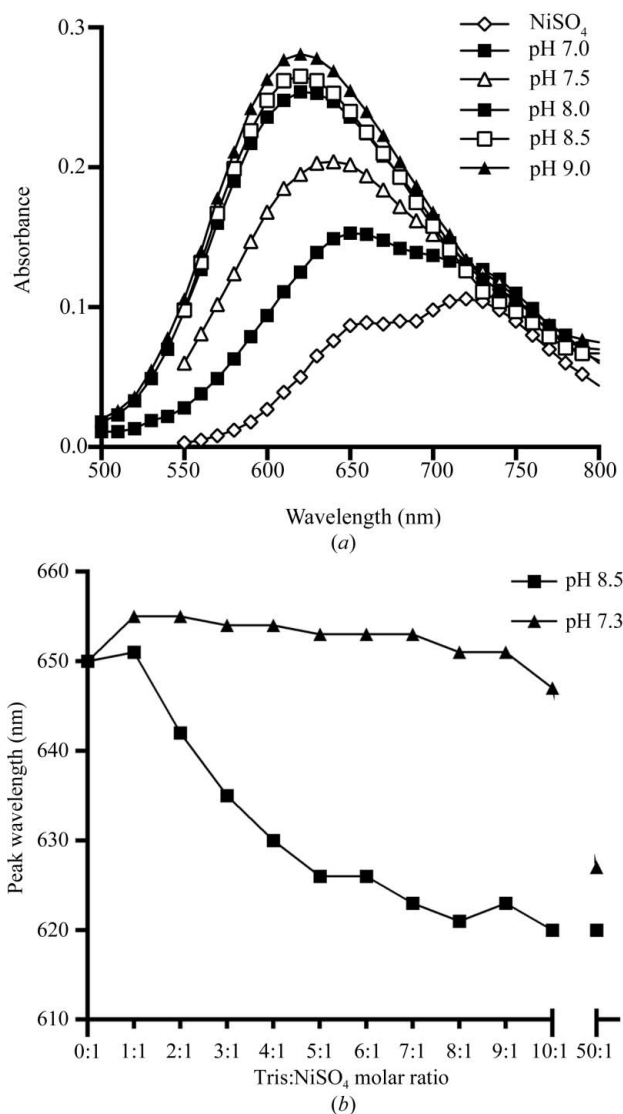

Figure 2
Formation of M^{2+}–Tris complexes at different pH values. (a) UV absorption spectra of Ni^{2+} ions (50 mM) in aqueous solutions containing 500 mM Tris at different pH values were collected between 500 and 800 nm. The formation of Ni–Tris complexes leads to a hypsochromic shift of the absorption peak wavelength. (b) Variation of the peak wavelength of the Ni^{2+}–Tris complex as a function of the molar ratio between ion and ligating groups.

drastically compared with that observed in the presence of a nonchelating buffer. Indeed, with the exception of Mn^{2+}, the binding of metal ions to the enzyme active site is enhanced in the presence of Tris, as judged from the lower K_i values (Table 3). Instead, the addition of Tris reduced the affinity of the ions for the enzyme–substrate complex, as shown by the increase in K_{ii}. The evidence that metalorganic complexes bind to the active site of IAGNH is a novel finding, and these coordination structures could be used as a scaffold for the design of novel inhibitors that depart from substrate-like or transition-state-like structures.

3.4. Structural studies of IAGNH

In order to decipher the structural determinants mediating the high-affinity binding of competitive iminoribitol-based inhibitors, we determined the crystal structures of IAGNH unbound and in complex with the compounds ImmA (IAGNH-ImmA), UAMC-000363 (IAGNH-363) and UAMC-000312 (IAGNH-312) (Fig. 1 and Supplementary Fig. S1).
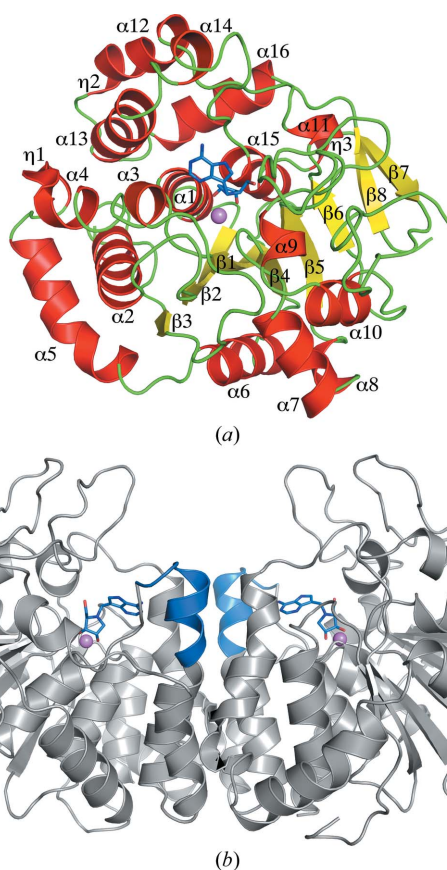
Figure 3
Structures of IAGNH. (a) Ribbon representation of the IAGNH monomer. The IAGNH-363 complex is shown with α-helices depicted as red ribbons, β-strands as yellow arrows and connecting loop regions in green. The active-site Ca^{2+} is shown as a violet sphere and the UAMC-00363 compound bound to the active site is shown as a stick model. Secondary-structure-element residues are labelled for reference; for their assignment, see Supplementary Fig. S2. (b) Structure of the IAGNH dimer. Ribbon representation of the functional dimer, with the region undergoing a conformational rearrangement upon active-site occupation coloured blue.

Moreover, we determined the structure of the enzyme in complex with Ni^{2+}–Tris (IAGNH-NiTris) in order to clarify the structural basis of the inhibition of IAGNH by metal ions and metalorganic compounds. An additional structure (IAGNH-312-M) obtained at basic pH in the presence of both a substrate-like molecule and an Ni^{2+} ion was determined to shed light on the mechanism of noncompetitive inhibition by divalent metal ions.

3.4.1. Overall IAGNH structure and structural rearrangements upon ligand binding. The IAGNH monomer displays the typical NH fold composed of 16 α-helices, eight β-strands and three 3_{10}-helices arranged in an open (αβ) structure with a mixed eight-stranded β-sheet surrounded by α-helices (Degano *et al.*, 1996; Fig. 3 and Supplementary Fig. S2). The active site of IAGNH is located at the topological switchpoint of the core β-sheet in a deep cavity with a Ca^{2+} ion octa-coordinated by the side chains of Asp10, Asp15 (bidentate) and Asp261 and the main-chain carbonyl of Thr137. The coordination sphere in the unliganded protein is completed by three water molecules, two of which are replaced by the O2′ and O3′ hydroxyls of iminoribitols upon inhibitor binding. The IAGNH enzyme crystallized in four distinct space groups with different asymmetric unit contents yet with a conserved homodimeric structure (Fig. 3). No major conformational differences can be observed upon superposing IAGNH with the homologous isozyme from *T. vivax* (r.m.s.d. of 0.54 Å for 244 homologous C^α positions). However, significant differences are apparent from the 6-oxopurine-specific isozyme IGNH, which can be aligned with unliganded IAGNH with an r.m.s.d. of 2.35 Å for 221 C^α atoms (Supplementary Fig. S2). The unliganded IAGNH assumes an open conformation with a solvent-accessible active site that rearranges upon binding competitive inhibitors to shield the reaction centre from the solvent *via* a structural rearrangement of residues 245–255 (referred to as loop 2; Fig. 3). This conformational change is reflected in a variation in contact surface at the dimer interface (980–1300 Å^2) owing to the formation of hydrogen bonds between the ordered loop 2 and the opposite monomer. This conformational change has also previously been reported for TvIAGNH and is directly involved in the catalytic process of the enzyme (Versees *et al.*, 2006).

3.4.2. Different modes of iminoribitol ring binding at a conserved active site. The compounds immucillin-A (ImmA), UAMC-00363 (363) and UAMC-00312 (312) all contain an iminoribitol moiety, yet the aglycone is directly linked to the C1′ atom in ImmA and to the N4′ nitrogen *via* a methylene bridge in the others (Fig. 4 and Supplementary Fig. S3). In all of the structures the 2′-OH and 3′-OH of the ligand coordinate the catalytic Ca^{2+} ion. The position occupied by the 3′-OH is strictly conserved, but the 2′-OH in the IAGNH-ImmA complex is shifted by ∼1.0 Å compared with the 363 and 312a structures yet maintains its interaction (2.6 Å) with the active-site ion. The different positioning of the iminoribitols leads to a near-superposition of the N4′ atom in 312 and 363 with the C1′ atom in ImmA (Fig. 4). As a consequence, the N4′ atom of ImmA is involved in a hydrogen-bonding interaction with the Asn186 side-chain amide carbonyl (3.1 Å), while this inter-

action is less favourable for the same atom in compounds 363 and 312, as the distance between the two atoms is increased to 4.0 Å. Thus, the different linkage between the iminoribitol ring and the aglycone in the compounds studied leads to different binding interactions between the amino sugar and the IAGNH active site, albeit mediated by the same amino-acid residues.

3.4.3. Comparison of interactions between IAGNH and the aglycone in N4′- and C1′-substituted iminoribitols.

The inhibitors studied here differ in (i) the linkage between the iminoribitol and the aglycone and (ii) the chemical features of the base-like moiety. The compounds bind similarly at the IAGNH active site, interacting with the Ca^{2+} ion and with a subset of amino-acid side chains using both the iminoribitol ring and the nitrogenous base (Supplementary Fig. S3). The purine-like aglycone of the inhibitors bound to IAGNH is consistently stacked between the indole side chains of Trp83

and Trp260. The base-like moiety of the compounds interacts with both IAGNH amino-acid residues and highly structured water molecules that are an integral part of the ligand-recognition system of the enzyme. We analyzed the differences between the modes of binding of these compounds in a pair-wise manner. ImmA and 363 are both endowed with a cova-lently bound 9-deazadenine aglycone, but at different atoms of the iminoribitol (C1′ and N4′, respectively; Fig. 1). The different linkages in the two compounds result in small variations in the protein–ligand interactions (Fig. 4). In both structures the protein and the base interact *via* hydrogen bonds between Asp40 and the N3 atom, and between Glu248 and Arg252 and the N6 amino group. Glu248 also interacts with the N1 atom of the base through a water-bridged hydrogen bond. Another water molecule is hydrogen-bonded to the N7 atom at a distance of 3.5 Å from Arg252. Notably, the interaction between Glu248 and the N6 amine in the IAGNH-363 complex is shorter compared with the ImmA-bound structure (3.0 *versus* 3.4 Å). The aglycone assumes different inclinations with respect to the plane of the indole ring of Trp260 that are followed by a small reorientation of the side chain of Trp83 to maintain a parallel π–π interaction and comparable distances to the aromatic systems. Compound 312 differs from compound 363 by the substitution of the N6 amino group with a carbonyl and of the N7 N atom with an S atom (Fig. 1), resulting in a tenfold increase in the inhibition constant towards IAGNH (Supplementary Table S3). Although compound 312 binds similarly to IAGNH compared with compound 363, it displays suboptimal interactions between its aglycone and the surrounding protein resi-dues and solvent molecules (Fig. 4). The O6 keto group of 312 establishes only one hydrogen-bonding interaction with the side chain of Arg252, which extends deeper into the active site to approach the electro-negative O atom. No interaction with Glu248 is observed, as it cannot accept a hydrogen bond from the O6 atom and thus reorients its side chain away from the base and towards the dimer interface. The N1 atom of the inhibitor maintains the inter-action with the water molecule observed in the ImmA and 363 complexes; however, in this structure it does not interact directly with Glu248. Moreover, the replacement of the endocyclic N7 with an S atom results in a weaker hydrogen-bonding interaction with the neighbouring water molecule, as judged by the increased distance. Taken together, these structural differences in binding interactions decrease the inhibitory potency of compound 312.
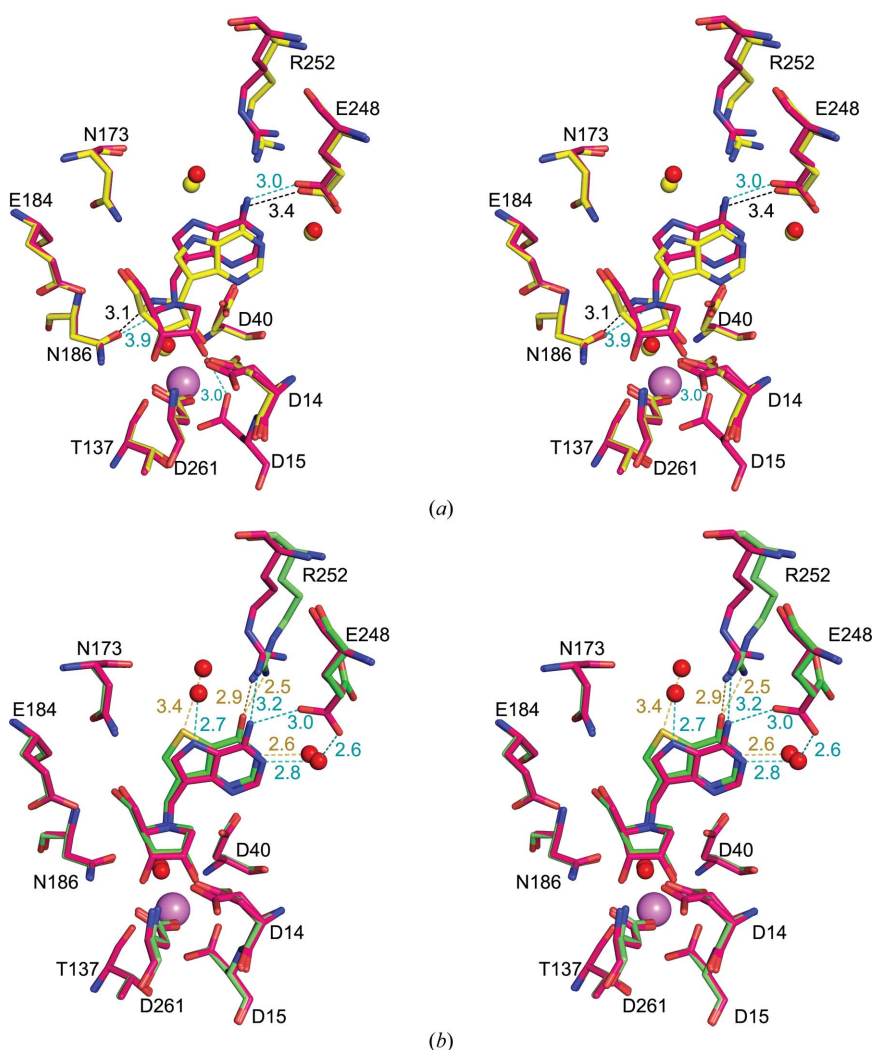

Figure 4
Comparison of the interactions of IAGNH with different inhibitors. (a) Superposition of the active site of IAGNH bound to ImmA (C atoms coloured yellow) and to 363 (C atoms coloured magenta). (b) Active site of IAGNH bound to inhibitor 363 (C atoms coloured magenta) or to 312 (C atoms coloured green). Enzyme–ligand contacts that differ in the compared enzyme–inhibitor complexes are shown as dashed lines (black for ImmA, cyan for 363 and orange for 312) and the distances are reported in Å. A full description of the individual contacts between IAGNH and the inhibitors is given in Supplementary Fig. S3.

3.4.4. Structural basis for loop 2 closure. Binding of ImmA, 363 or 312 to IAGNH induces the structuring of the otherwise flexible residues of loop 2 through a reorganization of specific interactions within the protein (Fig. 5). In the unliganded IAGNH Asp14 is involved in hydrogen bonds to both the side chain of Tyr257 and the indole ring of Trp242 via a bridging water molecule. Upon inhibitor binding, the Asp14 side chain rotates to establish a hydrogen bond with the iminoribitol 2′-OH. An additional conformation of Asp14 is observed in the IAGNH-363 complex, where it forms hydrogen bonds to the main chains of residues Trp260, Asp261 and Ala262. Regardless of the conformation, a repositioning of Asp14 allows the relocation of Tyr257 towards the core of the active site and its hydrogen-bonding to Asn12. In the process, several salt bridges are also formed and contribute to stabilizing the closed conformation. The guanidinium moiety of Arg252 approaches both Glu248 and Asp255, which are highly flexible in the unliganded structure. A salt bridge between Arg219 and Asp222 found in the unliganded IAGNH is replaced by a similar interaction between the basic residue and Glu249. The small movements of the side chains of Trp83 and Trp260 to optimize the stacking interactions with the aglycone are also likely to be relevant in driving the conformational change of loop 2, as are the previously described polar interactions between the loop 2 residues Glu248 and Arg252 and the purine-ring substituents.

3.5. Binding of the metalorganic Ni–Tris coordination complex to the IAGNH catalytic site

The finding that divalent transition-metal ions, as well as their coordination complexes with Tris, inhibit IAGNH was an unprecedented finding that warranted further structural investigation. The structure of IAGNH-NiTris shows one Ni–Tris coordination complex (1:1 stoichiometry) fully occupying the active site of the IAGNH enzyme and a closed conformation of the enzyme. The C^{α} atoms of the IAGNH-NiTris complex superpose on the IAGNH-ImmA and IAGNH-363 structures with r.m.s.d. values of 0.74 and 0.82 Å, respectively. The Tris molecule bound at the active site is hydrogen-bonded to the side chains of amino acids Asp14, Asp40, Asn173, Glu184 and Asp261, mimicking the previously described interactions between the IAGNH active site and the iminoribitols (Fig. 6). The nickel ion is coordinated in an octahedral geometry by the side chain of Asp14 and the amino group and two hydroxyls of the Tris molecule. The hexacoordination sphere is completed by two water molecules. The Ni^{2+} ion closely approaches the catalytic Ca^{2+}, with an average refined distance of 3.8 Å in the two independent crystallographic monomers. Binding of Ni–Tris induces ordering of loop 2, but this segment assumes a different conformation compared with the previously described complexes. The side chain of Asp14 rotates to coordinate the metal ion, allowing the conformational change. However, Tyr257 repositions its side chain further away from the active site, hydrogen-bonding to Asn12 via a ordered solvent molecule that superposes with the Tyr257 hydroxyl in the IAGNH-363 complex structure (Fig. 6).

Since no nitrogenous base mimic is present in the IAGNH-NiTris complex, the side chain of Arg252 moves deep into the catalytic site, establishing a cation–π interaction with the indole ring of Trp83 and driving the tip of loop 2 inside the active site core. Glu248 also relocates, yielding a single continuous helical segment between helices $\alpha13$ and $\alpha14$ with a canonical 3.0 Å hydrogen bond between the main-chain atoms of Met244 and Glu248 (Fig. 6). Hence, loop 2 assumes a different conformation when IAGNH is bound to Ni–Tris.

3.6. Noncompetitive inhibition of IAGNH by divalent metal ions

The overall IAGNH-312-M structure reveals striking differences when compared with the same enzyme–inhibitor complex obtained at lower pH (IAGNH-312). Firstly, the active site is partially occupied by an Ni–Tris molecule, albeit at low occupancy, bound to the enzyme as observed in the IAGNH-NiTris structure. Secondly, while the inhibitor 312 binds at the active site in a conformation that is substantially identical in the two complexes, the protein–ligand interactions differ. The binding of a single Ni^{2+} ion to the side chains of His247 from both molecules of the IAGNH dimer leads to a completely different arrangement of the residues of loop 2 that border the outer portion of the active site (Fig. 7). The O6 atom of the bound 312 does not interact with the side chains of residues Glu248 and Arg252; rather, it is within hydrogen-bonding distance of the main-chain N atoms of residues Glu248 and Glu249 (Fig. 7). As an additional consequence of the loop 2 rearrangement, different hydrogen-bonding interaction are formed between the IAGNH monomers. The main-chain carbonyl of Ser245 is hydrogen-bonded to the side-chain amide of residue Asn89 in the second monomer. Similarly, the
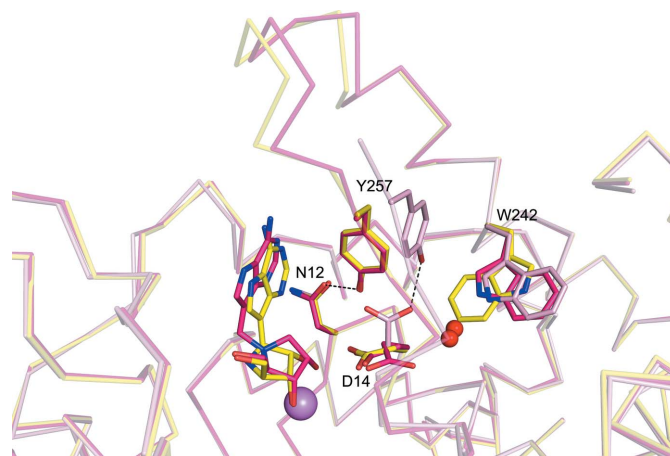

Figure 5
Mechanism of the rearrangement of loop 2 to the catalytic conformation upon transition-state-like inhibitor binding. The figure shows a superposition of the structures of unliganded IAGNH (C atoms coloured pink) and its complexes with compounds 363 (C atoms coloured magenta) and with ImmA (C atoms coloured yellow). The binding of inhibitor induces a flipping of the side chain of Asp12, which interacts with Tyr257 in the unliganded structure, to form a hydrogen bond to the iminoribitol. Tyr257 relocates to hydrogen-bond to Asn12. Trp242 may assume two different rotamers that are apparently unrelated to the loop 2 conformation.

side chain of Tyr257 reorients and interacts through its side-chain hydroxyl with the side chain of Asp92 from the opposing monomer (Supplementary Fig. S4). Thus, the binding of the divalent metal at the IAGNH monomer–monomer interface induces a different conformation of the catalytic loop compared with the transition-state complex, modifies the enzyme–substrate interactions and results in a rigidification of the interaction surface.
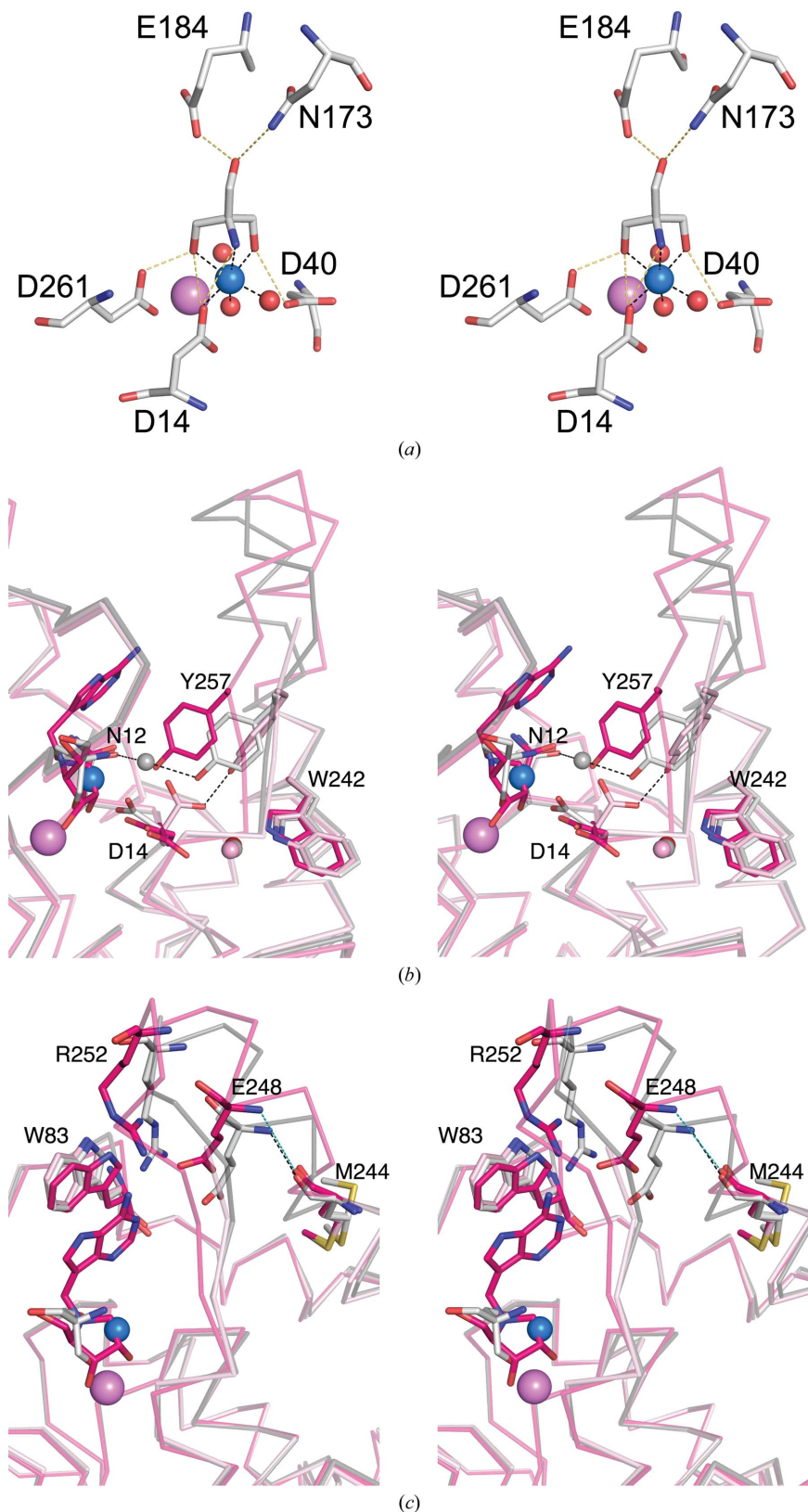
4. Discussion

Here, we report the biochemical and structural characterization of IAGNH from *T. brucei brucei*, the inhibition of which by specific compounds is expected to lethally interfere with the purine nucleotide metabolism of the parasite. Indeed, UAMC-00363 is a nanomolar inhibitor of IAGNH and displays trypanocidal activity both *in vitro* and *in vivo*, albeit likely mediated by interactions with multiple molecular targets (Berg, Kohl *et al.*, 2010).

The enzyme specificity clearly reflects an evolutionary optimization for the selection of substrates, both through binding and catalysis, that is a consequence of the purine auxotrophy of the parasite. The catalytic efficiency and inhibition pattern of the IAGNH parallels that previously observed for the homologous *T. vivax* isozyme (Goeminne *et al.*, 2008; Versées *et al.*, 2001). However, in *T. brucei* IAGNH the K_m and k_{cat} values are both approximately tenfold higher for purine nucleosides. Both isozymes are inhibited by immucillins and *N*-arylmethyl iminoribitols, but the compounds tested so far bind less efficiently to the *T. brucei* IAGNH active site compared with the *T. vivax* counterpart, with K_i values that are between fourfold and 40-fold higher. These findings are surprising, since these compounds were designed using

(a)

(b)

(c)

Figure 6
Structural basis for the competitive inhibition of IAGNH by Tris coordination complexes. (*a*) Interactions between the Tris molecule and the active site of IAGNH. Hydrogen bonds are shown as dashed lines. (*b*) Coordination of the Ni^{2+} ion by active-site residues and ordered solvent molecules. (*c*) Binding of Ni–Tris induces a different conformational change in IAGNH. When Ni–Tris binds to the active site of IAGNH, Tyr257 relocates in an intermediate position between that observed in the unliganded and, for instance, the 363-bound complex. The side chain of Tyr257 still establishes a hydrogen bond to the side chain of Asn12, albeit mediated by a water molecule found at the same site where the Tyr257 hydroxyl relocates in the other complexes. (*d*) The upper portion of the loop 2, in the absence of the ligand aglycone, interacts with IAGNH residues to stabilize an extended $\alpha12$ helix and preventing the attainment of the catalytic conformation.

TvIAGNH, which shares 63% sequence identity, as a molecular target. This underscores that during the process of drug design the structural characterization to high resolution of the molecular target bearing the highest homology to that from the human pathogen is of paramount importance. Thus, the present crystal structures of *T. brucei brucei* IAGNH, which shares 100% primary-structure identity with the enzyme from the human pathogen *T. brucei gambiense*, are an absolutely essential tool for the rational development of compounds with therapeutic potential.

In *T. brucei brucei*, two distinct genes encode NH enzymes with partially overlapping substrate specificity, reflecting the essential role of purine-base recycling in the life cycle of the parasite. To ensure efficient functional inhibition of trypanosomal nucleotide catabolism, both enzymes must be simultaneously targeted by specific compounds. Both the IAGNH and IGNH enzymes display the overall NH fold (Supplementary Fig. S5) in an apparent case of divergent evolution of protein structure, since they share only 10% sequence identity. Differences can be appreciated in catalytic site composition (Supplementary Fig. S5), as the IAGNH sandwiches the substrate base between Trp83 and Trp260, an interaction that has been demonstrated to be essential for catalysis by TvIAGNH (Versées *et al.*, 2004). Two aromatic residues are also present in the active site of the IGNH, but are arranged differently in space, thus likely imposing a different mode of ligand binding (Vandemeulebroucke *et al.*, 2010). Striking differences are indeed apparent when looking at the inhibition of the two *T. brucei brucei* enzymes by iminoribitols. Immucillins are low-nanomolar inhibitors of both enzymes, but N4′-substituted iminoribitols display 10^3-fold higher K_i values for the IGNH (Supplementary Table S3). Thus, the existing differences between IGNH and IAGNH can be exploited for the design of isozyme-specific competitive inhibitors. Further studies of the interactions between the IGNH and inhibitors may help to clarify the structural basis for these differences in binding affinities.

The catalytic cycle of NH enzymes, irrespective of their specificity and their structural homology group (Giabbai & Degano, 2004), takes advantage of conformational changes to perform catalysis (Degano *et al.*, 1998; Fornili *et al.*, 2010; Versees *et al.*, 2006). The open structure of NHs allows access of substrates to the catalytic site cavity, while the closed conformation is optimal for transition-state stabilization. Based on the present structures, a molecular explanation for the initiation of the conformational change can be put forth. In the unliganded IAGNH, residue Tyr257 is hydrogen-bonded to Asp14 to lock the terminal part of loop 2 in a conformation that hinders the structuring of the flexible region. Upon active-site occupation, Asp14 rotates about the C^α—C^β bond to interact with the ligand, allowing Tyr257 to relocate towards the active-site core. When a base-mimicking ligand is present, residue Arg252 from loop 2 interacts with the substituent at C6, driving the bending of the terminal part of helix α13 and resulting in the formation of a direct hydrogen bond between Tyr257 and Asn12. In the absence of a base mimic, such as in the complex with Ni–Tris, Arg252 interacts with Trp83, and Tyr257 occupies a site that is intermediate between the unliganded structure and the transition-state complex, establishing a water-mediated hydrogen bond with Asn12. Hence, the loss of the interaction between Asp14 and Tyr257 is
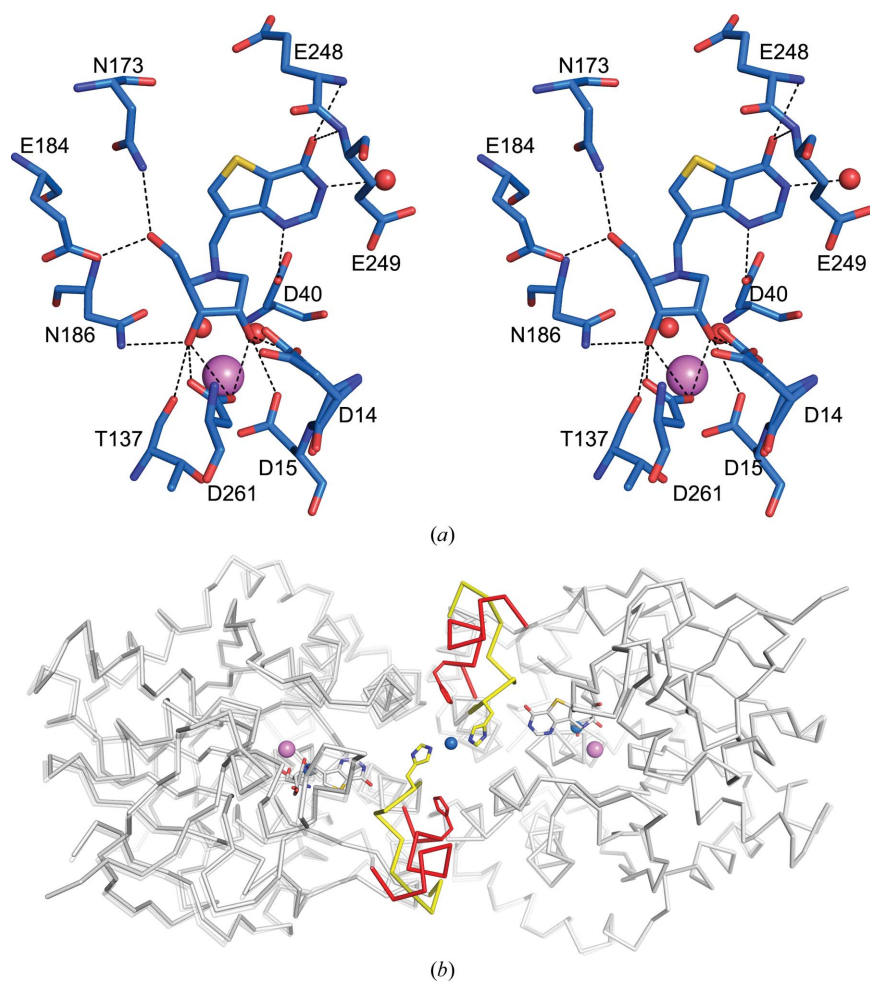
Figure 7
Structural basis for noncompetitive inhibition of IAGNH by divalent metal ions. (*a*) Stereo image of the interactions between IAGNH and compound 312 when Ni^{2+} is bound at the monomer–monomer interface of the enzyme. The keto group at position C6 of the inhibitor base moiety establishes contacts with the main-chain N atoms of residues Glu248 and Glu249. These contacts differ from those observed in the absence of the interface-bound ion, as shown in Fig. 4. (*b*) Binding of Ni^{2+} at the dimer interface is mediated by chelation by His247 from both monomers and stabilizes a different conformation of loop 2. The structures of IAGNH bound to 312-M and 363 are superimposed and shown as a grey ribbon. The loop 2 region is coloured yellow for the 312-M structure and red for the 363 complex. His247 is shown as a stick model, with the C atoms coloured following the same scheme. The 312 compound is shown in sticks and the active-site Ca^{2+} is shown as a violet sphere.

necessary to allow the conformational change in IAGNH. Tyr257 must then directly hydrogen-bond to Asn12 to achieve the catalytic conformation of loop 2, yet it can also occupy alternative positions, induced by the nature of the ligand, that result in a different conformation of the polypeptide segment. The reorientation of the Trp242 side chain, which has been proposed to be crucial for structuring loop 2 in TvIAGNH (Versées *et al.*, 2009), is not necessary for the conformational change in the *T. brucei* isozyme, since a different orientation of the side-chain indole compared with the unliganded protein is only observed in the ImmA and 312 structures, while it is retained in the other complexes. In summary, IAGNH can assume different stable conformations of loop 2 that are induced by interactions with active-site ligands bearing distinct chemical features. It is hence conceivable that specific inhibitors that specifically target different conformations of IAGNH could be designed.

The structures of IAGNH bound to three iminoribitol-based inhibitors help to define the important ligand features that ensure tight binding to the active site. A comparison of the ImmA and 363 structures underscores how the enzyme–iminoribitol and enzyme–base interactions concur in determining the binding affinity. The methylene bridge in compound 363 allows the base to optimally stack with Trp83 and the formation of a shorter hydrogen bond between the N6 amino group and residue Glu248. However, the iminoribitol ring adopts an N4'-*exo* conformation and is rotated compared with that observed in the IAGNH-ImmA complex, in which C4'-*endo* puckering of the iminoribitol is observed. As a consequence, the N4' atom of compound 363 displays weaker interactions with Asn186, while the O2' hydroxyl is closer to the side chain of Asp15. Thus, the position of the iminoribitol N4' atom at the active site is of primary importance for tight binding. The optimization of hydrogen-bonding and stacking interactions between the aglycone and the enzyme appears to be essential to achieve the highest affinity. Indeed, compounds 312 and 363 differ only in two atoms at the base-mimicking moiety, yet the K_i of the former is approximately tenfold higher. The substitution of the amino group of 363 by the ketone in 312 results in loss of hydrogen bonds, and the S atom at position 7 interacts weakly with the surrounding solvent molecules owing to its electronegativity. To corroborate the hypothesis of the role of hydrogen bonds to the nitrogenous base, compound UAMC-00109 has a keto group at position 6 and its K_i is 30 n*M*, while compound UAMC-00375 which only bears the S atom has an increased K_i of 56 n*M*. The synergistic effect of the simultaneous substitutions leads to the difference in contacts observed in the IAGNH-312 structure that translate into a K_i of 190 n*M*. Hence, optimal inhibition of IAGNH should take advantage of adequate positioning of the mimic of the transition-state positive charge and interactions with residues from loop 2 approaching the ligand and may further benefit from polar functional groups protruding from position 7 of the purine ring. Further characterization of the thermodynamics of inhibitor binding to IAGNH is required to validate the role of the enthalpic contribution to the inhibition constant.

The finding that metalorganic complexes can inhibit NH enzymes is unprecedented and provides new insights into the molecular details of their active-site properties. The IAGNH-bound Ni^{2+} ion bears a positive charge, which is likely to be partially shielded by the chelating O and N atoms from the Tris and solvent molecules, yet the ion can approach the active-site Ca^{2+} (3.7 Å) and occupy the ribosyl-binding site, approximately centred on the C1'—O4' bond of the substrate. Thus, the positively charged ion apparently mimics the main feature of the NH-catalyzed reaction: a partial oxonium-ion character at this bond in the transition state (Horenstein & Schramm, 1993). It is thus conceivable that other organic compounds bearing positive charges may be effective as ribosyl mimics. The interactions between Ni–Tris and IAGNH are mediated solely by the amino acids at the bottom of the active site, yet the enzyme undergoes a tightening of its structure, confirming that the flipping of the side chain of Asp14 is sufficient for transition to a closed conformation. We have previously described how a small variation of the aglycone structure can significantly modulate the binding of iminoribitols to IAGNH. Thus, the inclusion of a nitrogenous base mimic directly linked to the Tris molecule may greatly enhance the inhibition constant of the metalorganic complex. In summary, although metal-coordination complexes are unlikely to enter the drug-design phase owing to their potential toxicity to the host, the IAGNH-NiTris structure suggests a new chemical scaffold for the design of new inhibitors. This approach, albeit in the reverse direction, has been used, for instance, in the development of ruthenium-containing kinase inhibitors derived from the organic compound staurosporine (Maksimoska *et al.*, 2008). Compounds that depart from nucleoside-like structures may be of interest to avoid cross-reactivity with other host proteins.

Even in the absence of Tris the divalent metal ions exert an inhibitory effect on IAGNH, with mechanisms of inhibition ranging from mixed to noncompetitive. The competition of divalent cations with substrate demonstrates that the active site of NHs exerts an attractive effect towards positively charged compounds, albeit likely solvated and with a partially shielded charge. This is somewhat surprising since a divalent Ca^{2+} ion is constitutively bound to the active site of these enzymes. Nevertheless, this finding is consistent with the ability of the NH active site to stabilize a partial positive charge at the transition state. The K_i values for the metal ions do not correlate with their ionic radii; for instance, Cu^{2+} and Zn^{2+} have a similar radius yet the former does not bind to the IAGNH active site. As expected, the addition of metal-chelating agents such as glycylglycine abolishes inhibition by the ions. Addition of Tris instead decreases the K_i for Co^{2+} and Ni^{2+}, which is likely to be owing to the formation of a more effective M^{2+}–Tris competitive inhibitor. Further structural studies are expected to shed light on the mode of binding of cations to the IAGNH active site.

Noncompetitive inhibition arises from binding of a compound to the enzyme–substrate complex, preventing catalysis and reducing the maximum velocity of the enzymatic reaction. Cu^{2+} ions are outstanding noncompetitive inhibitors

of IAGNH, with a submicromolar K_{ii} value, while the other ions bind less tightly. This finding that M^{2+}–Tris complexes are poorer noncompetitive inhibitors of IAGNH suggests that the ion optimally binds to the enzyme–substrate complex without assistance from other chelating agents. We could not detect the presence of ions that could exert a noncompetitive inhibitory effect upon soaking of unliganded IAGNH crystals with divalent cations, underscoring the requirement for the presence of a substrate analogue at the active site for the binding of the divalent cation. Indeed, an Ni^{2+} ion bound at the dimer interface was only apparent when the protein was cocrystallized in the presence of the weaker inhibitor 312. The structure of the ternary complex showed differences in the loop 2 conformation and in monomer–monomer interactions compared with the IAGNH-312 complex. In both structures Asp14 releases Tyr257 upon binding of the substrate to allow the restructuring of loop 2. However, in the ternary complex His247 coordinates the Ni^{2+} ion and locks the loop 2 conformation to prevent the interaction between Tyr257 and Asn12 that is necessary to reach the transition-state structure. Thus, the observed noncompetitive inhibition by divalent metal ions is mediated by the stabilization of a 'noncatalytic' loop 2 conformation. The role of His247 is supported by the pH dependency of the K_{ii} value for Cu^{2+}, which is greater than 1 mM at pH 6.5 but sharply decreases to 1 μM at pH 7.5, advocating the involvement of a residue with near-neutral pK_a, such as a solvent-exposed His residue.

5. Conclusions

The high-resolution crystal structures of IAGNH from *T. brucei* bound to different inhibitors clarify the structural basis for tight-binding inhibition and are mandatory templates for the design of second-generation compounds with trypanocidal activity. Novel leads may be designed based on the IAGNH-NiTris complex to depart from substrate-like and transition-state-like structures to enhance inhibitor selectivity. The novel noncompetitive inhibition by divalent ions, as well as further insights into the conformational changes accompanying catalysis in IAGNH, deepen our understanding of the mechanism of action of this important class of enzymes.

References

Allen, D. E., Baker, D. J. & Gillard, R. D. (1967). *Nature (London)*, **214**, 906–907.

Barrett, M. P., Mottram, J. C. & Coombs, G. H. (1999). *Trends Microbiol.* **7**, 82–88.

Berens, R. L., Marr, J. J., LaFon, S. W. & Nelson, D. J. (1981). *Mol. Biochem. Parasitol.* **3**, 187–196.

Berg, M., Kohl, L. et al. (2010). *Antimicrob. Agents Chemother.* **54**, 1900–1908.

Berg, M., Van der Veken, P., Goeminne, A., Haemers, A. & Augustyns, K. (2010). *Curr. Med. Chem.* **17**, 2456–2481.

Berriman, M. et al. (2005). *Science*, **309**, 416–422.

Brun, R., Don, R., Jacobs, R. T., Wang, M. Z. & Barrett, M. P. (2011). *Future Microbiol.* **6**, 677–691.

Cassera, M. B., Hazleton, K. Z., Merino, E. F., Obaldia, N., Ho, M. C., Murkin, A. S., DePinto, R., Gutierrez, J. A., Almo, S. C., Evans, G. B., Babu, Y. S. & Schramm, V. L. (2011). *PLoS One*, **6**, e26916.

Chen, V. B., Arendall, W. B., Headd, J. J., Keedy, D. A., Immormino, R. M., Kapral, G. J., Murray, L. W., Richardson, J. S. & Richardson, D. C. (2010). *Acta Cryst.* D**66**, 12–21.

Cohen, S. X., Ben Jelloul, M., Long, F., Vagin, A., Knipscheer, P., Lebbink, J., Sixma, T. K., Lamzin, V. S., Murshudov, G. N. & Perrakis, A. (2008). *Acta Cryst.* D**64**, 49–60.

Degano, M., Almo, S. C., Sacchettini, J. C. & Schramm, V. L. (1998). *Biochemistry*, **37**, 6277–6285.

Degano, M., Gopaul, D. N., Scapin, G., Schramm, V. L. & Sacchettini, J. C. (1996). *Biochemistry*, **35**, 5971–5981.

Emsley, P. & Cowtan, K. (2004). *Acta Cryst.* D**60**, 2126–2132.

Emsley, P., Lohkamp, B., Scott, W. G. & Cowtan, K. (2010). *Acta Cryst.* D**66**, 486–501.

Estupiñán, B. & Schramm, V. L. (1994). *J. Biol. Chem.* **269**, 23068–23073.

Fischer, B. E., Häring, U. K., Tribolet, R. & Sigel, H. (1979). *Eur. J. Biochem.* **94**, 523–530.

Fornili, A., Giabbai, B., Garau, G. & Degano, M. (2010). *J. Am. Chem. Soc.* **132**, 17570–17577.

French, S. & Wilson, K. (1978). *Acta Cryst.* A**34**, 517–525.

Gandhi, V., Kilpatrick, J. M., Plunkett, W., Ayres, M., Harman, L., Du, M., Bantia, S., Davisson, J., Wierda, W. G., Faderl, S., Kantarjian, H. & Thomas, D. (2005). *Blood*, **106**, 4253–4260.

Giabbai, B. & Degano, M. (2004). *Structure*, **12**, 739–749.

Giblett, E. R., Ammann, A. J., Wara, D. W., Sandman, R. & Diamond, L. K. (1975). *Lancet*, **1**, 1010–1013.

Goeminne, A., Berg, M., McNaughton, M., Bal, G., Surpateanu, G., Van der Veken, P., De Prol, S., Versées, W., Steyaert, J., Haemers, A. & Augustyns, K. (2008). *Bioorg. Med. Chem.* **16**, 6752–6763.

Gopaul, D. N., Meyer, S. L., Degano, M., Sacchettini, J. C. & Schramm, V. L. (1996). *Biochemistry*, **35**, 5963–5970.

Hall, J. L., Swisher, J. A., Brannon, D. G. & Liden, T. M. (1962). *Inorg. Chem.* **1**, 409–413.

Hammond, D. J. & Gutteridge, W. E. (1984). *Mol. Biochem. Parasitol.* **13**, 243–261.

Horenstein, B. A. & Schramm, V. L. (1993). *Biochemistry*, **32**, 9917–9925.

Iovane, E., Giabbai, B., Muzzolini, L., Matafora, V., Fornili, A., Minici, C., Giannese, F. & Degano, M. (2008). *Biochemistry*, **47**, 4418–4426.

Jackson, A. P., Sanders, M., Berry, A., McQuillan, J., Aslett, M. A., Quail, M. A., Chukualim, B., Capewell, P., MacLeod, A., Melville, S. E., Gibson, W., Barry, J. D., Berriman, M. & Hertz-Fowler, C. (2010). *PLoS Negl. Trop. Dis.* **4**, e658.

James, D. M. & Born, G. V. (1980). *Parasitology*, **81**, 383–393.

John, D. T. & Petri, W. A. Jr (2006). *Markell and Voge's Medical Parasitology*, 9th ed. Philadelphia: Elsevier Health Sciences.

Kabsch, W. (2010a). *Acta Cryst.* D**66**, 125–132.

Kabsch, W. (2010b). *Acta Cryst.* D**66**, 133–144.

Koning, H. P. de, Bridges, D. J. & Burchmore, R. J. (2005). *FEMS Microbiol. Rev.* **29**, 987–1020.

Kuettel, S., Greenwald, J., Kostrewa, D., Ahmed, S., Scapozza, L. & Perozzo, R. (2011). *PLoS Negl. Trop. Dis.* **5**, e1164.

Kuettel, S., Mosimann, M., Mäser, P., Kaiser, M., Brun, R., Scapozza, L. & Perozzo, R. (2009). *PLoS Negl. Trop. Dis.* **3**, e506.

Lee, B. & Richards, F. (1971). *J. Mol. Biol.* **55**, 379–400.

Legros, D., Evans, S., Maiso, F., Enyaru, J. & Mbulamberi, D. (1999). *Trans. R. Soc. Trop. Med. Hyg.* **93**, 439–442.

Maksimoska, J., Feng, L., Harms, K., Yi, C., Kissil, J., Marmorstein, R. & Meggers, E. (2008). *J. Am. Chem. Soc.* **130**, 15764–15765.

Mazzella, L. J., Parkin, D. W., Tyler, P. C., Furneaux, R. H. & Schramm, V. L. (1996). *J. Am. Chem. Soc.* **118**, 2111–2112.

Miles, R. W., Tyler, P. C., Evans, G. B., Furneaux, R. H., Parkin, D. W. & Schramm, V. L. (1999). *Biochemistry*, **38**, 13147–13154.

Murshudov, G. N., Skubák, P., Lebedev, A. A., Pannu, N. S., Steiner, R. A., Nicholls, R. A., Winn, M. D., Long, F. & Vagin, A. A. (2011). *Acta Cryst.* D**67**, 355–367.

Murshudov, G. N., Vagin, A. A., Lebedev, A., Wilson, K. S. & Dodson, E. J. (1999). *Acta Cryst.* D**55**, 247–255.

Ogbunude, P. O., Ikediobi, C. O. & Ukoha, A. I. (1985). *Ann. Trop. Med. Parasitol.* **79**, 7–11.

Pace, C. N., Vajdos, F., Fee, L., Grimsley, G. & Gray, T. (1995). *Protein Sci.* **4**, 2411–2423.

Parkin, D. W. (1996). *J. Biol. Chem.* **271**, 21713–21719.

Parkin, D. W., Horenstein, B. A., Abdulah, D. R., Estupinan, B. & Schramm, V. L. (1991). *J. Biol. Chem.* **266**, 20658–20665.

Parkin, D. W., Limberg, G., Tyler, P. C., Furneaux, R. H., Chen, X. & Schramm, V. L. (1997). *Biochemistry*, **36**, 3528–3534.

Perrakis, A., Sixma, T. K., Wilson, K. S. & Lamzin, V. S. (1997). *Acta Cryst.* D**53**, 448–455.

Schramm, V. L. (2002). *Biochim. Biophys. Acta*, **1587**, 107–117.

Tsuboi, K. K. & Hudson, P. B. (1957). *J. Biol. Chem.* **224**, 889–897.

Vagin, A. & Teplyakov, A. (2010). *Acta Cryst.* D**66**, 22–25.

Vandemeulebroucke, A., Minici, C., Bruno, I., Muzzolini, L., Tornaghi, P., Parkin, D. W., Versées, W., Steyaert, J. & Degano, M. (2010). *Biochemistry*, **49**, 8999–9010.

Versées, W., Barlow, J. & Steyaert, J. (2006). *J. Mol. Biol.* **359**, 331–346.

Versées, W., Decanniere, K., Pellé, R., Depoorter, J., Brosens, E., Parkin, D. & Steyaert, J. (2001). *J. Mol. Biol.* **307**, 1363–1379.

Versées, W., Goeminne, A., Berg, M., Vandemeulebroucke, A., Haemers, A., Augustyns, K. & Steyaert, J. (2009). *Biochim. Biophys. Acta*, **1794**, 953–960.

Versées, W., Loverix, S., Vandemeulebroucke, A., Geerlings, P. & Steyaert, J. (2004). *J. Mol. Biol.* **338**, 1–6.

Versées, W. & Steyaert, J. (2003). *Curr. Opin. Struct. Biol.* **13**, 731–738.

Vodnala, M., Fijolek, A., Rofougaran, R., Mosimann, M., Maser, P. & Hofer, A. (2008). *J. Biol. Chem.* **283**, 5380–5388.

Winn, M. D. *et al.* (2011). *Acta Cryst.* D**67**, 235–242.

World Health Organization (1998). *Control and Surveillance of African Trypanosomiasis*. Geneva: World Health Organization. http://whqlibdoc.who.int/trs/WHO_TRS_881.pdf.

World Health Organization (2006). *Wkly Epidemiol. Rec.* **81**, 71–80.